



HAL
open science

Observing gravitational redshift with X-Ray emission in galaxy clusters with Athena X-IFU

Alexei Molin, Nicolas Clerc, Étienne Pointecouteau, François Pajot, Edoardo Cuchetti

► **To cite this version:**

Alexei Molin, Nicolas Clerc, Étienne Pointecouteau, François Pajot, Edoardo Cuchetti. Observing gravitational redshift with X-Ray emission in galaxy clusters with Athena X-IFU. *Astronomy and Astrophysics - A&A*, 2023, 679, pp.A24. 10.1051/0004-6361/202347269 . hal-04229395

HAL Id: hal-04229395

<https://hal.science/hal-04229395>

Submitted on 9 Nov 2023


HAL is a multi-disciplinary open access archive for the deposit and dissemination of scientific research documents, whether they are published or not. The documents may come from teaching and research institutions in France or abroad, or from public or private research centers.

L'archive ouverte pluridisciplinaire **HAL**, est destinée au dépôt et à la diffusion de documents scientifiques de niveau recherche, publiés ou non, émanant des établissements d'enseignement et de recherche français ou étrangers, des laboratoires publics ou privés.



Distributed under a Creative Commons Attribution 4.0 International License

Observing gravitational redshift with X-ray emission in galaxy clusters with *Athena* X-IFU

A. Molin¹ , N. Clerc¹, E. Pointecouteau¹, F. Pajot¹, and E. Cucchetti²

¹ IRAP, Université de Toulouse, CNRS, CNES, UT3-PS, Av. du Colonel Roche 9, 31400 Toulouse, France
e-mail: alexei.molin@irap.omp.eu

² Centre National d'Etudes Spatiales, Centre spatial de Toulouse, 18 avenue Edouard Belin, 31401 Toulouse Cedex 9, France

Received 23 June 2023 / Accepted 5 September 2023

ABSTRACT

Context. The Doppler shift predicted by general relativity for light escaping a gravitational potential has been observed on Earth as well as in the direction of various stars and galaxy clusters at optical wavelengths.

Aims. Observing the gravitational redshift in the X-ray band within galaxy clusters could provide information on their properties and, in particular, their gravitational potential. We present a feasibility study of such a measurement, using the capabilities of the next-generation European X-ray observatory *Athena*.

Methods. We used a simple generalized Navarro–Frenk–White potential model along with a β -model for the density of baryonic matter, which sets the emission to provide an estimation of the observed redshift in the simplest of cases. We generated mock observations with the *Athena* X-ray Integral Field Unit (X-IFU) for a nearby massive cluster, while seeking to recover the gravitational redshift along with other properties of the toy model cluster.

Results. We investigated the observability of the gravitational redshift in an idealized test case of a nearby massive cluster with the *Athena* X-IFU instrument, as well as its use in probing the properties of the potential well. We were also able to constrain the mass to a $\sim 20\%$ level of precision and the cosmological redshift to less than $\sim 1\%$, within a simplified and idealized observational framework. More refined simulations accounting for further effects such as the internal gas motions and the actual shape of the potential well are required to fully investigate the feasibility of measuring the gravitational redshift for a single target or statistically over a sample of galaxy clusters.

Key words. X-rays: galaxies: clusters – gravitation

1. Introduction

Gravitational redshift is caused by the loss of energy of a photon emitted within a gravitational potential and traveling through it. This effect is predicted by general relativity (Einstein 1916) as well as by most alternative gravity theories (Cataneo & Rapetti 2018). The effective associated redshift is given by $\Delta\Psi/c^2$, where $\Delta\Psi$ is the difference in the gravitational potential between the point of emission and the observer, which is mainly the potential due to the mass of the considered astrophysical object along the line of sight. Hence, the measurement of this redshift can be used to probe either the potential or, equivalently, the mass distribution from which it derives.

Clusters of galaxies, as the most massive gravitationally bound objects in the Universe, are reasonable candidates for the observation of this effect. Some of the earliest predictions for such observations in clusters of galaxies appear in Cappi (1995) and Broadhurst & Scannapieco (2000). Measurements through optical spectra soon followed, as in Wojtak et al. (2011) or, more recently, Mpetha et al. (2021) and Rosselli et al. (2023). A comprehensive overview is provided in Sect. 4 of Cataneo & Rapetti (2018), which focuses on tests of gravity with galaxy clusters. In that same section, the authors discuss the observability of the gravitational redshift from X-ray spectra of clusters of galaxies, suggesting that future instruments might be able to achieve such measurements.

The X-ray emission from the intracluster medium (ICM) in galaxy clusters arises mainly from the radiative cooling of the

hot gas infalling within the halo potential well (Sarazin 1988). The ICM is routinely observed in X-rays from the center of clusters to their outskirts (Ettori et al. 2019; Walker et al. 2022). This hot gas is highly ionized and shows strong emission lines from the various elements within it. These emission lines offer access to high precision measurements of the redshift through high resolution spectroscopy (Hitomi Collaboration 2016). It is thus suited for the observation of the gravitational redshift as (at first order), the hot gas distribution follows that of the dark matter, which is the main source of the halo gravitational well. Mapping the weak signal expected from gravitational redshift requires (i) high resolution X-ray spectroscopy in order to retain a high precision over the redshift determination and (ii) a spatial resolution mapping capability to trace the gravitational redshift induced gradient from the center to the cluster's outer parts.

Current X-ray missions such as *XMM-Newton* or *Chandra* only provide one of these products at a time, with either low-spectral-resolution imagers such as EPIC (Turner et al. 2001) and ACIS (Garmire et al. 2003) or high-spectral-resolution dispersive spectrometers such as RGS (den Herder et al. 2001) and LETG/HETG (Brinkman et al. 2000; Canizares et al. 2005). The upcoming generation of X-ray observatory will carry integral field unit spectrometers to offer the capability to achieve spatially resolved high-spectral resolution observation in X-rays. The Resolve instrument (Ishisaki et al. 2022) on board the XRISM missions (Tashiro et al. 2020) will soon fly, although the observation of the outer parts of clusters will likely be very limited due to the modest size of the XRISM mirrors impeding the

measurement of small redshift gradients. The X-ray Integral Field Unit (X-IFU, hereafter) on board the *Athena* observatory implements the science theme of the “hot and energetic Universe” (Nandra et al. 2013) and it should provide the adequate performances. The X-IFU is required to have a 5 arcmin field of view (FoV) with a full width half maximum (FWHM) resolution of 5 arcsec and a spectral resolution of 2.5 eV over the 0.2–7 keV energy range (Barret et al. 2018, 2023). With this work, we investigate the feasibility of measuring the gravitational redshift in massive clusters of galaxies with the X-IFU instrument.

The work and results presented in this paper were obtained with the current baseline configuration for the *Athena* mission. Because of the actual programmatic context, the European Space Agency is revisiting the formulation of the *Athena* mission science case and specifications. Our results may thus be affected by the to-be-defined instrumental configuration of the *Athena* mission. Throughout this study, we assume a Λ CDM cosmology with $h = H_0/100 \text{ km s}^{-1} \text{ Mpc}^{-1} = 0.7$, $\Omega_\Lambda = 0.7$ and $\Omega_m = 0.3$. In this framework, at a redshift of $z = 0.1$, 10 kilo-parsecs (kpc) correspond to an angular extent of 5.4 arcsec.

2. X-IFU/*Athena* mock observations

In order to investigate the observability of the gravitational redshift from the X-ray emission of galaxy clusters, we used a cluster toy model, based on the simulations presented in Cucchetti et al. (2018b), to produce simulated observations with *Athena* X-IFU using the SIXTE instrument end-to-end simulator (Wilms et al. 2014; Dauser et al. 2019). The emission models and spectral fitting rely on the *xspec* software (Arnaud 1996).

2.1. The X-IFU instrument

As a next-generation European X-ray observatory, *Athena* (Barcons et al. 2017), will board an integral field unit spectrometer with unprecedented capabilities, the X-IFU. It will allow for the spatial mapping of emission lines over extended sources such as galaxy clusters, allowing for spatially resolved spectroscopy with a power of $R \sim 1000$ (Barret 2022). The X-IFU will be equipped with a high precision detection chain including an array of more than a thousand Transition Edge Sensors (TES) cooled to 55 mK and high precision readouts electronics. It will provide the required high-spectral-resolution of 2.5 eV FWHM over the 0.2–7 keV energy band. Combined with the large collective area of the *Athena* mirrors, it will benefit from an effective area of $\sim 1 \text{ m}^2$ at 1 keV. The requirement for the spatial resolution of the *Athena* mirrors is 5 arcsec half energy width (HEW). Taken together, these performances will fully open the era of spatially resolved high spectral resolution at X-ray wavelengths, in the wake of the first glimpses provided by the SXS instrument onboard the Hitomi satellite and of the upcoming observation of the Resolve instrument (Sato et al. 2023) on board the XRISM mission (XRISM Science Team 2022).

2.2. Cluster toy model

For the purpose of our study, we chose to model a nearby massive cluster, with $z = 0.1$ and $M_{200} = 10^{15} M_\odot$. Accounting for the faintness of the gravitational redshift effect, local and very massive clusters are ideal targets to aim at its detection. Lower and/or more distant clusters would render such detection almost impossible and, as such, they are not further considered in this

study. A more detailed discussion on the cluster choice is provided in Sect. 3.1. The parameters of the cluster according to the model described below are summarized in Table 1. The angular size of the cluster at this distance, noted θ_{200} , is provided as well.

The cluster toy model consists of a gas density model and a dark matter density model. The cluster is discretized as a grid of emitting particles, to which the parameters of the emission model are assigned based on their position in the cluster. The size of the grid is chosen such that it contains one X-IFU FoV and is deep enough to contain R_{200} of the cluster along the line of sight. At the chosen redshift, this corresponds to a grid of 7500 kpc in depth (i.e., along the line of sight), and 938×938 kpc in width.

2.2.1. Redshift

The redshift of photons emitted in the cluster is the composition of multiple sources, which are detailed with the following equations from Cataneo & Rapetti (2018), for the emission point \mathbf{x} and an observer lying at the origin of the reference frame:

$$1 + z_{\text{tot}} = (1 + z_{\text{cosmo}}) \left[1 + \frac{1}{c^2} (\Psi(0) - \Psi(\mathbf{x})) + \frac{\mathbf{n} \cdot \mathbf{v}}{c} + \frac{v^2}{2c^2} \right] \quad (1)$$

where z_{cosmo} is the cosmological redshift, Ψ is the gravitational potential, \mathbf{n} is the unitary vector parallel to the line of sight, and \mathbf{v} is the velocity vector of the emitting point relative to the observer. The two last terms correspond respectively to the Doppler shift along the line of sight and the relativistic transverse Doppler shift. In the ICM, these are mainly due to the bulk and turbulent motions of the gas. We deliberately chose not to address these intrinsic motions of the gas in our study (we further discuss this choice in Sect. 5). The resulting approximation is then:

$$z_{\text{grav}} = \frac{\Delta\Psi}{c^2}. \quad (2)$$

2.2.2. Dark matter density model

We assumed that the dark matter (DM) density follows a generalized Navarro Frank White radial profile (hereafter, gNFW). The gNFW profile has been worked out based on a generalization of the NFW profile (Navarro et al. 1997; Nagai et al. 2007). The gNFW profile has three slope indexes, α , β , and γ , where β is the inner slope and γ is the outer one. We used a version presented in Zhu et al. (2019), which sets α and β to 1. The profile is otherwise characterized by r_s , a scale radius, the overdensity, δ_c , and γ is the asymptotic slope when $r \rightarrow 0$. The scale radius, r_s , is related to the mass, M_δ , at the density contrast, δ , (different from the overdensity) times the critical density of the Universe at redshift z , $\rho_{\text{crit}}(z)$, as follows:

$$r_s = \left(\frac{M_\delta}{\frac{4}{3}\pi\delta\rho_{\text{crit}}(z)} \right)^{\frac{1}{3}} \frac{1}{c_\delta}, \quad (3)$$

with c_δ being the concentration parameter. The overdensity, δ_c , can be expressed as a function of M_δ as follows:

$$\delta_c = \frac{M_\delta}{\int_0^{R_\delta} \frac{4\pi r^2 \rho_{\text{crit}}(z)}{(r/r_s)^\gamma (1+r/r_s)^{3-\gamma}}}, \quad (4)$$

with $R_\delta = c_\delta \cdot r_s$. This expression can be developed in the case of a gNFW density profile, as provided in the Appendix A. This entirely describes the DM density from which the gravitational potential can be derived analytically (Zhu et al. 2019).

Table 1. Parameters of our toy model clusters for the gravitational potential, DM and gas densities, and the gas emission.

Parameter	Value
M_{200}	$1 \times 10^{15} M_{\odot}$
$R_{200}(\theta_{200})$	2 Mpc (18.5')
c_{200}	4.5
γ	1.2
z_{cosmo}	0.1
r_c	400 kpc
β	$2/3$
n_0	$3 \times 10^{-3} [\text{cm}^{-3}]$
$k_B T$	7 [keV]
Abundance (Z/Z_{\odot})	0.7
n_H	$0.03 [10^{22} \text{cm}^{-2}]$

In doing this, we neglect the contribution of the gas and stars to the gravitational potential. We use this model in the following sections. We also chose to add a constant to the potential ϕ to set $\phi(r \rightarrow +\infty) = 0$. This allows for a straightforward conversion between the potential and the redshift of light emitted from a point \mathbf{r} in the cluster such that $z = \Psi(\mathbf{r})/c^2$ or, when expressed as an equivalent velocity shift, $v_z = \Psi(\mathbf{r})/c$.

2.2.3. Gas density model

We modeled the emission of our toy model cluster ICM with a broadened APEC model (bapec) under xspec (Smith et al. 2001). This model represents the emission of a collisional, optically thin, diffuse plasma, mainly through the Bremsstrahlung radiation for the continuum, as well as the atomic lines due to the different processes at play in the plasma (e.g., dielectronic recombination, ionization, and radiative transitions). The broadening of the lines is only thermal in our simulations, excluding other possible sources of broadening such as bulk motions or turbulence.

For this study, we restrained ourselves to a simple isothermal cluster with homogeneous abundance through the cluster. We set the temperature such that $k_B T = 7 \text{ keV}$. The solar abundances follows that of Anders & Grevesse (1989) and we set the intra-cluster gas global abundance such that $Z/Z_{\text{solar}} = 0.7$. This leaves only the redshift and the normalisation as varying parameters for the bapec model.

The norm of each emitting volume element, V , of the cluster is defined as:

$$N = \frac{10^{-14}}{4\pi(D_A(1+z))^2} \int n_e n_p dV, \quad (5)$$

with D_A as the angular distance of the cluster in cm, z as the cosmological redshift, n_e and n_p as the electron and proton particle densities in cm^{-3} , respectively. The resulting norm is given in photons per unit of volume, per unit of effective area, thus: cm^5 . For a fully ionized plasma, we can consider $n_e = 1.2n_p$. The emission model is multiplied by a photo-absorption model, phabs under XSPEC, using cross-sections from Verner et al. (1996), to account for the Galactic absorption. We fixed the hydrogen column density, noted n_H , to $0.03 \times 10^{22} \text{ cm}^{-2}$.

For analytical convenience, we adopted a simple β -model (Cavaliere & Fusco-Femiano 1976) as our gas density model, although it is not the best fit to represent the actual distribution



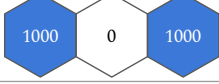



Layout	
Uniform Exposure 1	
Uniform Exposure 2	
Mixed Exposure 1	
Mixed Exposure 2	
Single Field	

Fig. 1. Observing strategies considered in our simulations. The layout of the X-IFU pointings is shown in the right column together with the exposure time for each pointing in ks. The count map for the configuration “uniform exposure 1” is plotted in the first line and shows the cluster center.

of the intra-cluster gas. It is parameterized by the core electron density, n_0 , the core radius, r_c , and the slope, β .

2.3. Foreground and background emissions

We accounted for the astrophysical foreground and background emissions in our simulations following the model proposed by McCammon et al. (2002). It includes a non absorbed thermal model representing the local bubble (apec), a second absorbed one for the Galactic halo (phabs*apec), and an absorbed power law for the cosmic X-ray background (CXB, phabs*powerlaw). We adopted the parametrisation provided by Lotti et al. (2014). The hydrogen column density is kept at the same value as for the cluster model.

The instrumental background is also accounted for in our simulations. It is managed entirely by the SIXTE tool according to the X-IFU requirements of $5 \times 10^{-3} [\text{counts s}^{-1} \text{ cm}^{-2} \text{ keV}^{-1}]$. This instrumental background mainly results from the high-energy cosmic rays hitting the neighborhood of the detector.

2.4. Observational strategies

We investigated various observational configurations in order to assess the feasibility of measuring the gravitational redshift with the X-IFU instrument on board Athena. We varied the number of X-IFU pointings from one to three and individual exposures from 125 ks (kiloseconds) to 1 Ms. The six investigated configurations are illustrated in Fig. 1. The various multiple pointings configurations allow us to sample measurements of the ICM emission as far as the characteristic radius of $\sim 0.6R_{200}$ ($\sim 0.9R_{500}$).

3. Mock data analysis

The main output of the SIXTE simulator is a mock event list of the X-IFU observation. For all the recorded events, namely, the X-ray photons that have been detected, the measured energy,

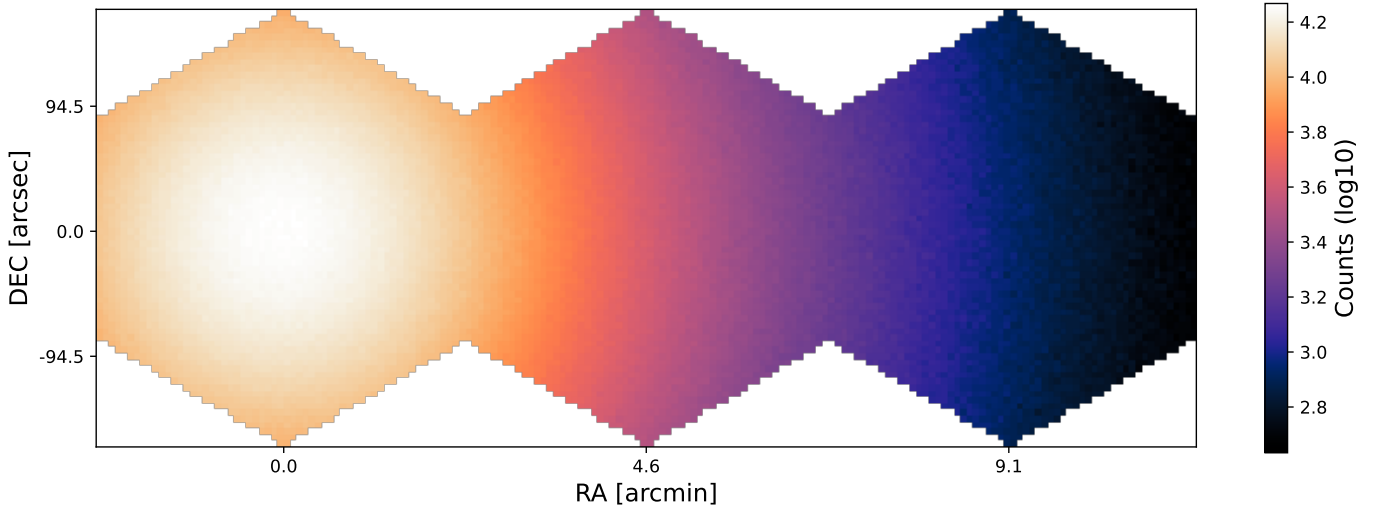


Fig. 2. Count map in each pixel ($\sim 5 \times 5$ arcsec) of three adjacent 1 Ms pointings of X-IFU (corresponding to uniform exposure 1 in Table 1) of a $10^{15} M_{\odot}$ and $z = 0.1$ cluster. The color scale is in units of \log_{10} of the counts. The center of the cluster is at (RA, Dec) = (0, 0)

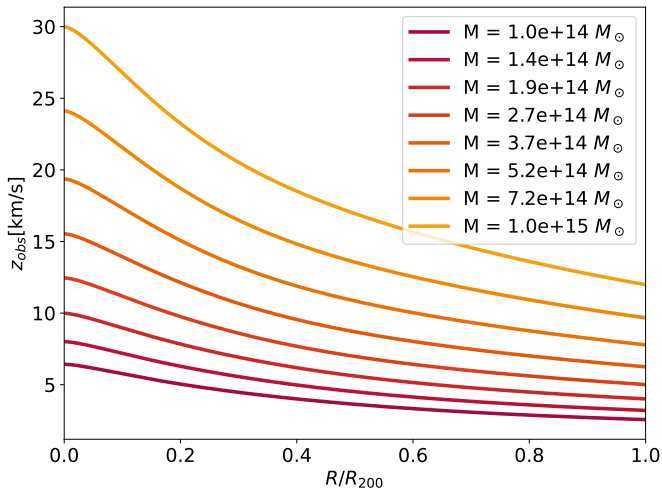


Fig. 3. Emission weighted radial profiles of the gravitational redshift for clusters of different masses.

detector and sky coordinates, time of arrival, and so on, are provided. From the SIXTE mock event lists, we generated count images. The spectra were computed within concentric annuli of constant width or over full X-IFU FoV. Each spectrum is fitted using `xspec` with the `phabs*baptec` model and the aforementioned model for the background, with the redshift, the cluster emission normalisation, temperature, abundance, and the background emission normalisations as free parameters. The velocity broadening of the `baptec` model, which is set to 0 when simulating the cluster emission, is also set to 0 during the fit. The justification for this choice is discussed in Sect. 3.2. From the best-fit value in each bin, we reconstructed the redshift profile used to assess the gravitational redshift. In Fig. 2, we show an example of a count map for an observation of three contiguous pointings (i.e., the configuration named “uniform exposure 1”, as defined in Fig. 1).

3.1. Modeling the observed gravitational redshift

From the DM potential well and gas emission models described in Sects. 2.2.2 and 2.2.3, we modeled the observed redshift as

an emission-weighted redshift along the line of sight. Then, it is expressed as:

$$z_{\text{obs,los}}(\theta) = \frac{\int_l z(\mathbf{r})\epsilon(\mathbf{r})dl}{\int_l \epsilon(\mathbf{r})dl}, \quad (6)$$

with $\epsilon(\mathbf{r})$ as the emissivity at \mathbf{r} , l as the line of sight, and θ as the angular distance to the cluster center. The finite dimension of the grid for the cluster model restricts the precision of the integrals to a finite length. We quantified that the loss in flux due to this cut-off is less than 1% by computing the integrals of the emissivity for different cutoff values. We approximate the integrals with a double exponential quadrature integral (Takahasi & Mori 1974), which allows for a very good approximation (within numerical errors) and important computational time improvement. The redshift in a single bin is obtained with:

$$z_{\text{bin}} = \frac{\int_{S_{\text{bin}}} z_{\text{obs,los}}(\theta)\epsilon_{\text{obs,los}}(\theta)d\theta}{\int_{S_{\text{bin}}} \epsilon_{\text{obs,los}}d\theta}, \quad (7)$$

with S_{bin} the area of the bin and $\epsilon_{\text{obs,los}} = \int_l \epsilon(\mathbf{r})dl$. This formula remains true for any bin shape.

Models of the observed scaled radial profile for the gravitational redshift, z_{obs} , are shown on Fig. 3 as a function of the cluster mass. As expected, more massive clusters show a deeper and steeper potential, making them obvious target for measurements of the gravitational redshift. The drawback is the angular size and extent of the cluster in view of the X-IFU FoV, limiting the emission sampling in the outer parts of clusters in a single X-IFU pointing. Even when the emission of more distant (hence, less extended) clusters at a given mass would be better sampled spatially, it quickly suffers from the dimming of the X-ray flux with redshift. The need for a balance between apparent luminosity and angular size, led us to choose a local massive cluster as a test case for our study.

3.2. Line shift measurements and fitting procedure

Figure 3 shows how the measurement of the gravitational redshift in a nearby massive cluster requires to measure redshifts with a precision of a few km s^{-1} . This is almost an order of

magnitude lower than the line shift expected from bulk motions and turbulence in the ICM (Kunz et al. 2022; Simionescu et al. 2019). The requirement on the line shift and line broadening precisions for the X-IFU in its current configuration is respectively of 10 and 20 km s⁻¹ (1 σ level), for a typical observation time of \sim 100 ks. This imposes the need for an energy scale precision to better than 0.4 eV at \sim 6 keV (1 σ level) and set over the 0.2–7 keV energy range (e.g., 0.4 eV/6 keV $\cdot c \simeq$ 20 km s⁻¹ at \sim 6 keV Cucchetti et al. 2018a). This means that no incoming photon can have its energy determined with a precision better than 0.4 eV. It should not, however, be interpreted as a strict limitation on line energy and, thus, the line speed measurements. Over a whole observation, the factors leading to the variation of the energy scale will be corrected every few ks (currently 4 ks considered for the X-IFU), and are expected to vary evenly around the 0 point. This means that over a typical observation time (i.e., 10–1000 ks), the energy scale variations should mainly result in a broadening of the lines. Assuming that other instrumental systematics are under control, the uncertainty on the line shift will be the only one remaining. It should remain below 10 km s⁻¹ for a 100 ks exposure time observation. It may thus be neglected in our 1 Ms simulations. We also note that the current version of SIXTE does not implement the effect of this in-flight energy scale correction.

For a given spectral resolution, given enough time, any precision over a Gaussian line centroid can be achieved. The associated error on the line centroid, σ_v , goes as $\sigma_v \sim \sigma_{\text{res}}/S/N$ (with S/N as the signal-to-noise ratio, typically the square root of the number of counts for photon noise). Hence, the only restriction for measuring line shifts, for a given resolution, is observing time, or conversely, for a given observation time, is the instrumental resolution. The approximation over the centroid given previously is true for a Gaussian line (see Cucchetti 2019, for extended details).

Besides the physical motivation of introducing thermal broadening, the reason for choosing the bapec model over a simple apec model is practical. The main contributing element for the redshift measurement in the fitting procedure is the lines. In the case of a simple APEC model, the lines are considered as infinitely thin. This means that fitting the line position is automatically limited by the energy bin width of the instrument’s response. More precisely, the likelihood becomes discretized and usual fitting procedures, such as gradient descent, do not guarantee proper convergence and/or proper parameter error estimation. We expand on this issue and illustrate it with a plot in Appendix C. However, with broadened lines (as is the case for a bapec model), this problem does not arise, and we can be confident in the fitting procedure and its outcome for the redshift. Hence, we used a bapec model for modeling and fitting the emission of the cluster. The velocity broadening was set to 0 in both cases, leaving only the thermal broadening accounted for.

Our spectra are binned according to the Kaastra & Bleeker (2016) method. They are then fitted over the whole X-IFU energy band, namely, 0.2–12 keV. We chose to make use of the whole information carried by the many emission lines of the ICM. We considered that this maximizes the use for the lines signal to extract the redshift. In the case of a real cluster (or a more evolved model), this would also allow for enough precision to be provided on the redshift with varying density, temperature, and abundances depending on the regions of the cluster investigated (i.e., central parts or outskirts). A focus on a single specific strong line (e.g., Fe K- α) could also deliver a constrained enough estimation of the gravitational redshift. However, such a investigation is beyond the scope of this paper.

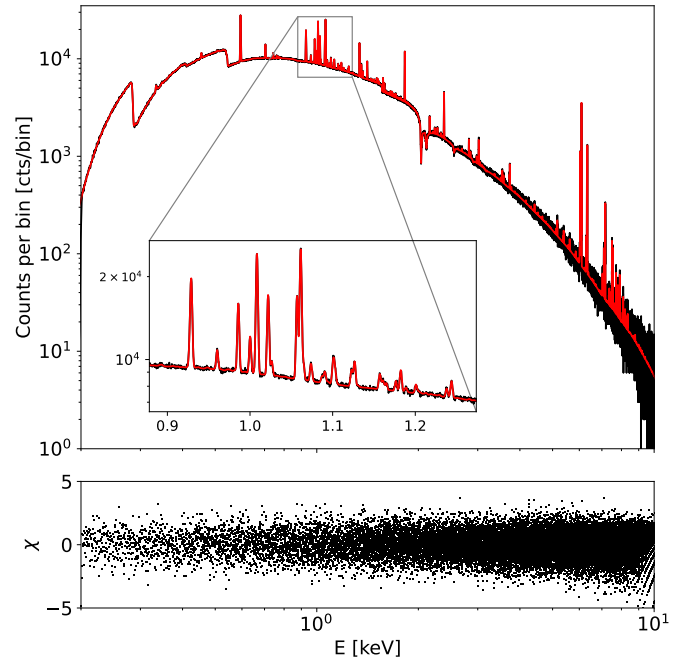


Fig. 4. Simulated spectrum from a 1Ms observation of the center of our cluster toy model (black line) and its best fit (red line). This spectrum is extracted from the central bin of the circular binning shown in the summary table in Fig. 1. An inset figure shows the details of the lines observed around 1 keV. The lower panel shows the error in units of χ for each bin. The quantized shape observed at the highest energies comes from the low number counts observed at these high energies.

4. Results

In this section, we first evaluate the precision in the construction of the redshift profile that is achievable for a simple, single X-IFU 1 Ms pointed observation of our toy model cluster. This allows for an evaluation of the reproducibility of such a measurement. In the second part, we investigate other observational strategies, using multiple X-IFU pointings and exposures to evaluate whether the observed redshift profile can be used as a probe to constrain parameters of the gravitational potential. We show an example the spectrum obtained with a 1Ms observation of the center of the cluster in Fig. 4.

4.1. Recovery of the gravitational redshift

From the various observing configurations of single or multiple X-IFU pointings as defined in Sect. 2.4, we are able to retrieve the radial profile for the redshift. The Poisson noise in our simulations is the only stochastic process. To check the reproducibility of our reconstructed redshift profile with respect to this source of noise, we ran 100 simulations for our “single-field” observational configuration. Figure 5 shows the mean profile and its dispersion over the 100 reconstructed profiles, together with a single profile with its error bars derived from the xspec fit. The profiles are reconstructed over ten circular concentric annuli from the cluster center and covering the whole FoV. The conversion to velocities shown on the y-axis assumes a prior knowledge of the cosmological redshift (z_{cosmo} in Eq. (1)). This exercise of reproducibility illustrates the dispersion of profiles, which is not fully encapsulated within the error bar of each single measurement. This exercise has been led only for this specific configuration because of its heavy computational demand (about 2 h

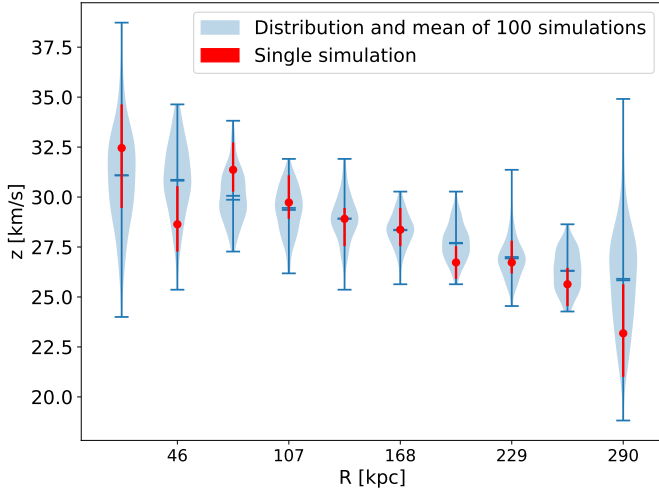


Fig. 5. Reproducibility in the reconstruction of the radial profile of the gravitational redshift over a single X-IFU pointing at the center of our toy model cluster. The blue points and associated errors show the mean profile and its associated dispersion over a 100 simulations of a 1Ms observation (see Sect. 4.1). The red points show the example of a single profile and the associated errors provided by *xspec*.

for a single simulation on 32 cores CPUs, hence, a total of about 200 h for the reproducibility study on a single toy model cluster). However, changing the binning and/or exposure time should not affect the recovery of the profile on average.

4.2. Constraining the cluster parameters

The gravitational redshift directly links to the halo potential well and, thereby, to the underlying total mass of the cluster. The measurement of the gravitational redshift profile can thus be used as a probe to determine the cluster mass. The assumption of a prior and perfect knowledge of the cosmological redshift allows for one of the parameters of the model to be fit, such as the cluster mass. We can fit the expected redshift profile from the model detailed in Sect. 3.1 to the redshift profile obtained from our mock observations. As a toy model, we used a simple least squares minimization for the fitting procedure. Figure 6 shows the distribution of the 100 best-fit curves, fitting only the mass of the cluster. The distribution of the best-fit profiles is centered on the expected input profile, showing little to no bias in the profile recovery. This idealistic situation leads to an exceedingly optimistic estimation of the halo mass. We obtained a mean best-fit mass of $0.998 \pm 0.018 \times 10^{15} M_{\odot}$ (for an expected mass of $10^{15} M_{\odot}$).

In reality, the situation would be less optimistic as none of the cluster parameters (e.g., the density, temperature, shape of the DM distribution, etc.) would be known perfectly. As such, they will have to be determined from the X-ray observations or constrained from ancillary data. The cosmological redshift could for instance be constrained from optical observations. The precision of this redshift would then condition our ability to estimate the gravitational redshift. All these uncertainties and unknowns would have to be formulated as priors in our analysis. As a first step towards this more complex situation, we considered the cosmological redshift to be completely undetermined. Because the mass and cosmological redshift similarly impact the observed redshift profile, we need to use the entire shape of the profile to disentangle their correlated effect (see, e.g., Fig. 3). To address this issue, we used multiple pointings mock observations (see

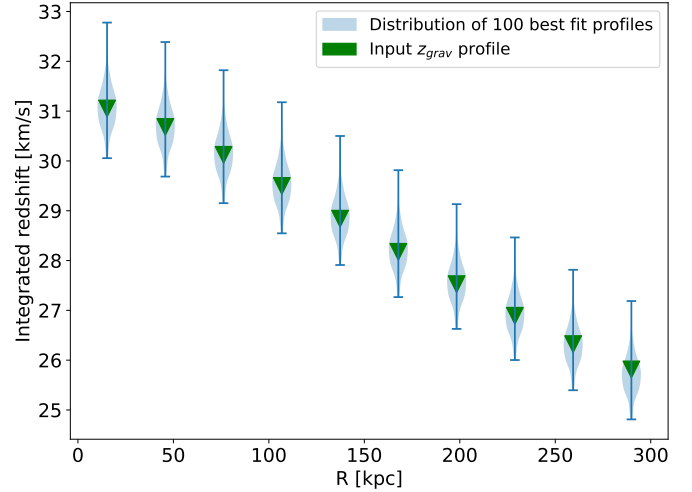


Fig. 6. Distribution of the best fit profiles to 100 simulated reconstructed gravitational redshift profiles from X-IFU mock observations. The expected profile, that was used as an input in all the simulations, is plotted with the green triangles.

Fig. 1). To maximize the signal-to-noise ratio (S/N) in the determination of the redshift, we considered each pointing of our three pointings configurations as a single bin and derived the associated spectra over the whole X-IFU FoV. In the case of a real potential well, small-scale variations in the gravitational field (and, thus, in the gravitational redshift distribution) could be expected, although this is not the case for our smooth gNFW toy model.

In the left panel of Fig. 7, we compare the posterior distribution for mass and redshift obtained with the Markov chain Monte Carlo (MCMC) method (using the *emcee* package) on three different observing configurations, with a single, two and three X-IFU pointings, respectively. The single pointing configuration is binned with ten circular annuli, whereas the two multiple pointings configurations are binned into a single region for each pointing. For the best case scenario, that is “uniform exposure 1”, the constraint obtained on the mass is $M = 0.80^{+0.17}_{-0.14} \times 10^{15} M_{\odot}$, whereas the single field alone provides $M = 0.63^{+0.58}_{-0.30} \times 10^{15} M_{\odot}$. The errors are provided at the 68% confidence level. While “uniform exposure 2” seems to be more centered on the true value, the first one brings more constraints and, thus, lower errors on the reconstruction of the mass and redshift due to the added third pointing (see Fig. 1). The shift with respect to the true values of the parameters is due to the sample variance, which affect both configurations similarly, each being a single statistical realisation of the cluster emission (see the reproducibility study in Sect. 4.1). We evaluated the Pearson correlation coefficient obtained over the mass and redshift samples in the distributions for each of these strategies. In all of them, the coefficient remains above 0.9 in absolute value. The strong degeneracy between the mass and redshift is only restrained to a smaller range for strategies mapping the outer parts of the cluster. In the presented case, the astrophysical and instrument backgrounds have little impact, as we have set relatively important exposure times and since we are targeting a nearby massive cluster (see Appendix B for further details on the simulations without background).

We also performed simulations with more realistic exposure times. In order to optimize the S/N across the radial range probed by our multiple pointings observations, we doubled the exposure time from one pointing to the next adjacent one (see Fig. 1:

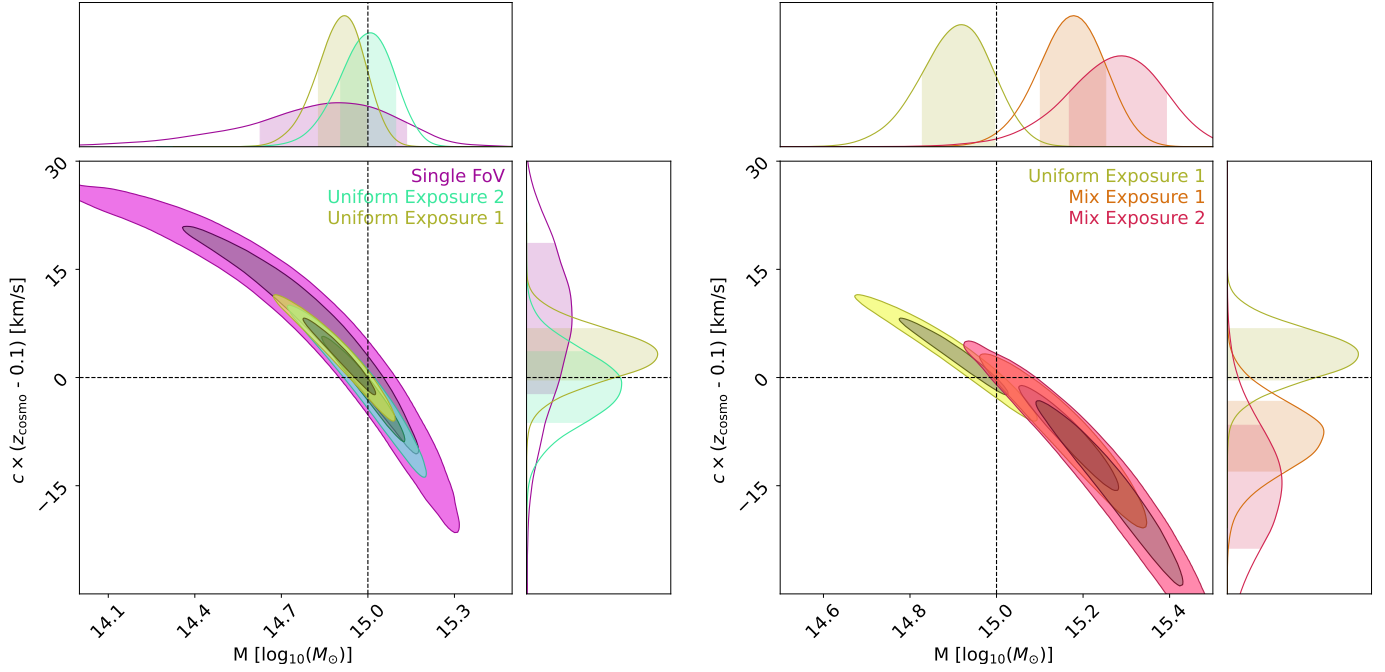


Fig. 7. Corner plots in the mass and redshift plane and associated posterior distribution for both parameters. The different colors correspond to the different observing strategies listed in the legend and presented in Fig. 1. Left: uniform exposures 1 and 2, compared with a single pointing observation. Right: mix exposures 1 and 2, compared with a single pointing observation. The input reference values are plotted as dotted lines.

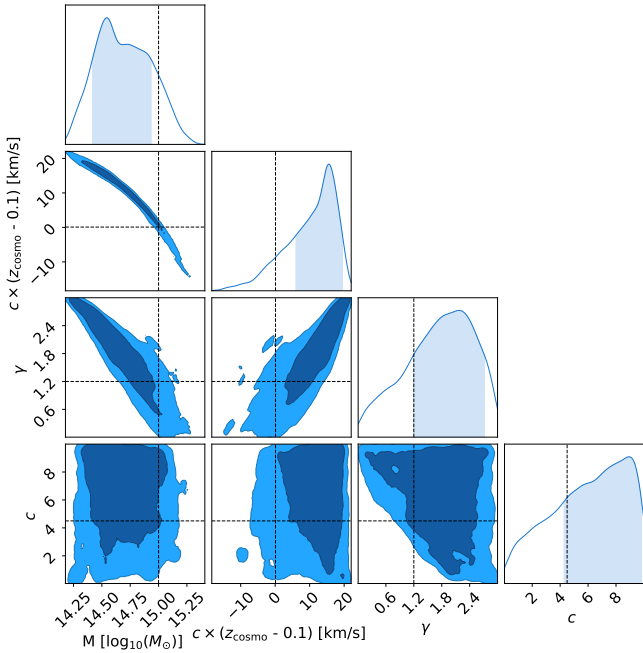


Fig. 8. Corner plot of the mass, redshift, γ and c_{200} gNFW parameters retrieved from the MCMC fit of the redshift profiles derived from the observing configuration named “uniform exposure 1”. The true values, used as input to the simulations, are plotted with dotted lines.

“mixed exposure 1” accounts for a total of 1.75 Ms exposure, whereas “mixed exposure 2” for a total of 875 ks. The results for these observing strategies are presented in the right panel of Fig. 7). “Mixed exposure 1” provides $M = 1.48^{+0.28}_{-0.23} \times 10^{15} M_{\odot}$ and “mixed exposure 2” provides $M = 1.84^{+0.56}_{-0.43} \times 10^{15} M_{\odot}$.

The posterior distribution retrieved from mixed exposures 1 and 2 in Fig. 7 are centered more than 1σ away from the

input values. We believe that the line of sight mixing causes an underestimation of the errors that cannot be accounted for by the `bapec` model under `xspec`. Because the likelihood used for the MCMC is using these very same errors from `xspec`, the retrieved parameter distribution is showing optimistic error levels. In addition, the mixed exposure 1 strategy gives a heavier weight to the pointings far from the center. This compensates the lower signal in these regions. However, the fit in these regions can be biased not only from the line of sight mixing but also from the stronger contribution of the background; hence, this encompasses a biased redshift measurement and a biased posterior distribution.

The previous tests assume that the shape of the potential was known, namely, that the parameters γ and c_{200} were fixed at their known input values. A final test was run freeing all the parameters of the gravitational potential, including the mass, γ , and c . The result is shown in Fig. 8. The distributions show that all the parameters span a large range of values, typical of unconstrained models. The concentration parameter, c is especially poorly constrained; it spans the entire uniform prior range, from 0 to 10. The upper left distribution shows the strong correlation between the mass and the cosmological redshift when the shape of the expected redshift profile is not fixed by the other shape parameters. This shows that the gravitational redshift alone cannot constrain all the parameters of the potential. We recall that it is highly unlikely that such measurements would be carried out from the X-ray point of view only, without any other ancillary data sets or inputs (e.g., gravitational lensing).

5. Conclusions and discussion

In this work, we evaluated the possibility of observing the gravitational redshift in galaxy clusters in X-rays with future integral field spectrometers such as the *Athena* X-IFU. To that end, we created mock observations of an idealized massive and nearby galaxy cluster (the targets with the highest probability to be

detected) with X-IFU, by using the SIXTE software. We analyzed the data with the xspec spectral analysis software. We reconstructed the gravitational redshift profile that we modeled through the shape of the cluster potential well and the X-ray emission of its gas content. We showed that: (1) X-IFU could recover the gravitational redshift for massive ($M_{200} \sim 10^{15} M_{\odot}$) and nearby ($z \sim 0.1$) clusters within a quite large, but still achievable exposure time; and (2) the measurement of the gravitational redshift profile can be used to derive properties of the halo gravitational potential, such as its total mass.

These conclusions have to take into account the limitations of our model. Firstly, we stress that the gas mass fraction in our simulated cluster is relatively high ($\sim 20\%$ for M_{gas}/M_{500} at R_{500}). This is due to our choice of a β -model for the gas distribution, which can overestimate the gas fraction at large radii. Moreover, our choice of total mass, that is $M_{200} = 10^{15} M_{\odot}$, is rather conservative with respect to some local massive clusters (Ettori et al. 2019). Assuming $M_{200} \approx 1.5 \times 10^{15} M_{\odot}$ would yield a gas fraction of about 15%. With such a cluster, we would observe a higher amplitude for the redshift profile. The mass does not affect the S/N of the observed X-ray spectra. Hence, this does not change the essence of our results, as the uncertainties come from the photon counts, and these are driven by the emission, exposure and distance.

Secondly, we neglected the motions of the gas in the cluster. These motions result in a Doppler shift in the emission, which is of the order of $\sim 100\text{--}1000 \text{ km s}^{-1}$ (Kunz et al. 2022; Simionescu et al. 2019). This is an order of magnitude above the observed redshift. It means that in a real cluster, the observation of the gravitational redshift would be added to that of bulk motion. The gravitational redshift would then be a difficult quantity to estimate. However, we can consider things the other way round, and any precise measurement of bulk or turbulent velocities using line shifts will have account for the gravitational redshift as a systematic bias. An a priori knowledge of the total mass profile, thus of the gravitational potential would provide the proper estimate of such a bias on bulk and turbulent motions of the ICM hot gas. In addition to turbulence, the internal structures of the physical properties of galaxy clusters (density, temperature, pressure, abundances, etc) depart at various scales from the idealized hypothesis of sphericity and homogeneity we adopted (e.g., Kravtsov & Borgani 2012; Lovisari & Maughan 2022).

The line of sight mixing is another issue when challenging the limits of spectral precision. Because the ICM is optically thin, we observe the emission of all the points along the line of sight. This increases the signal, but causes the different emitted spectra to be mixed. Because many of the observed quantities are not additive and we are modeling the observed spectrum with a single model, we assumed that the observed profile, which is an emission weighted average over different redshifts, is the profile of the emission weighted average redshift. This assumption works because the center of the cluster is the most emitting part and thus dominates the signal. However, this would not be systematically the case for a non-spherically symmetric potential and/or ICM emission. This obviously would also concern other physical parameters such as the temperature and the chemical abundance. The line of sight mixing remains a weak effect, as we illustrate in Fig. 4, where the observed spectrum is perfectly overlapping with the model. The evaluation of the fit of all our mock observations holds a $\chi^2/\text{d.o.f.}$ in the 1–1.15 range.

One way around these issues could be to stack several observations of different clusters. In doing that, fluctuations from cluster to cluster, such as the shape and the turbulence, could average out, and the gravitational redshift would remain. This would

then require scaling the clusters with respect to each other, as well as other practical considerations, such as the determination of the cluster center. Such investigations have already been done with optical data, and have been used to test alternative theories of gravity (Wojtak et al. 2011; Mpetha et al. 2021; Rosselli et al. 2023). Similar work could be undertaken on the basis of observations of clusters samples with future X-ray Integral Field Units, such as X-IFU.

By the time *Athena* X-IFU is launched, exploratory work could be carried out by the upcoming XRISM (XRISM Science Team 2022) mission and its Resolve instrument. The first high X-ray resolution spectra provided by its short lived predecessor, the SXS instrument onboard Hitomi (Sato et al. 2023), in the direction of the Perseus cluster held very promising perspectives on our ability to understand better the evolution and formation of galaxy clusters. There is hope that future data analysis methods will also be able to make full use of such spectra, allowing for combinations of spectral and spatial information in the cluster, and perhaps allow for the inclusion of the gravitational redshift as another useful probe to our understanding of these large structures.

At the time of publishing this paper, the European Space Agency has sponsored a full reformulation of the *Athena* mission science case and specifications. We thus stress that the results of our study may have to be reconsidered according to the future new instrumental requirements of the *Athena* mission.

Acknowledgements. We are grateful to the anonymous referee for fruitful comments that helped improving this paper. A.M., E.P. and N.C. acknowledge the support of CNRS/INSU and CNES. The following python packages have been used throughout this work : astropy (Astropy Collaboration 2013, 2018, 2022), chainconsumer (Hinton 2016), emcee (Foreman-Mackey et al. 2013), matplotlib (Hunter 2007) and cmasher (van der Velden 2020).

References

- Anders, E., & Grevesse, N. 1989, *Geochim. Cosmochim. Acta*, 53, 197
- Arnaud, K. A. 1996, in *Astronomical Data Analysis Software and Systems V*, eds. G. H. Jacoby, & J. Barnes, *ASP Conf. Ser.*, 101, 17
- Astropy Collaboration (Robitaille, T. P., et al.) 2013, *A&A*, 558, A33
- Astropy Collaboration (Price-Whelan, A. M., et al.) 2018, *AJ*, 156, 123
- Astropy Collaboration (Price-Whelan, A. M., et al.) 2022, *ApJ*, 935, 167
- Barcons, X., Barret, D., Decourchelle, A., et al. 2017, *Astron. Nachr.*, 338, 153
- Barret, D. 2022, 44th COSPAR Scientific Assembly, Held 16–24 July, 44, 2316
- Barret, D., Albuys, V., Herder, J.-W., d., et al. 2023, *Exp. Astron.*, 55, 373
- Barret, D., Lam Trong, T., den Herder, J. W., et al. 2018, in *Space Telescopes and Instrumentation 2018: Ultraviolet to Gamma Ray*, eds. J. W. A. den Herder, S. Nikzad, & K. Nakazawa, *SPIE Conf. Ser.*, 10699, 106991G
- Brinkman, B. C., Gunsing, T., Kaastra, J. S., et al. 2000, in *X-ray Optics, Instruments, and Missions III*, eds. J. E. Truemper, & B. Aschenbach, *SPIE Conf. Ser.*, 4012, 81
- Broadhurst, T., & Scannapieco, E. 2000, *ApJ*, 533, L93
- Canizares, C. R., Davis, J. E., Dewey, D., et al. 2005, *PASP*, 117, 1144
- Cappi, A. 1995, *A&A*, 301, 6
- Cataneo, M., & Rapetti, D. 2018, *Int. J. Mod. Phys. D*, 27, 1848006
- Cavaliere, A., & Fusco-Femiano, R. 1976, *A&A*, 49, 137
- Cucchetti, E. 2019, PhD Thesis, Université Paul Sabatier-Toulouse III, France
- Cucchetti, E., Eckart, M. E., Peille, P., et al. 2018a, in *Space Telescopes and Instrumentation 2018: Ultraviolet to Gamma Ray*, eds. J.-W. A. den Herder, S. Nikzad, & K. Nakazawa, *International Society for Optics and Photonics (SPIE)*, 10699, 106994M
- Cucchetti, E., Pointecouteau, E., Peille, P., et al. 2018b, *A&A*, 620, A173
- Dausser, T., Falkner, S., Lorenz, M., et al. 2019, *A&A*, 630, A66
- den Herder, J. W., Brinkman, A. C., Kahn, S. M., et al. 2001, *A&A*, 365, L7
- Einstein, A. 1916, *Ann. Phys.*, 354, 769
- Ettori, S., Ghirardini, V., Eckert, D., et al. 2019, *A&A*, 621, A39
- Foreman-Mackey, D., Hogg, D. W., Lang, D., & Goodman, J. 2013, *PASP*, 125, 306
- Garmire, G. P., Bautz, M. W., Ford, P. G., Nousek, J. A., & Ricker, G. R., Jr. 2003, in *X-ray and Gamma-ray Telescopes and Instruments for Astronomy*, eds. J. E. Truemper, & H. D. Tananbaum, *SPIE Conf. Ser.*, 4851, 28
- Hinton, S. R. 2016, *J. Open Source Softw.*, 1, 00045

- Hitomi Collaboration (Aharonian, F., et al.) 2016, *Nature*, **535**, 117
- Hunter, J. D. 2007, *Comput. Sci. Eng.*, **9**, 90
- Ishisaki, Y., Kelley, R. L., Awaki, H., et al. 2022, in *Space Telescopes and Instrumentation 2022: Ultraviolet to Gamma Ray*, eds. J. W. A. den Herder, S. Nikzad, & K. Nakazawa, *SPIE Conf. Ser.*, **12181**, 121811S
- Kaastra, J. S., & Bleeker, J. A. M. 2016, *A&A*, **587**, A151
- Kravtsov, A. V., & Borgani, S. 2012, *ARA&A*, **50**, 353
- Kunz, M. W., Jones, T. W., & Zhuravleva, I. 2022, in *Handbook of X-ray and Gamma-ray Astrophysics*, eds. C. Bambi, & A. Santangelo, 56
- Lotti, S., Cea, D., Macculi, C., et al. 2014, *A&A*, **569**, A54
- Lovisari, L., & Maughan, B. J. 2022, in *Handbook of X-ray and Gamma-ray Astrophysics*, eds. C. Bambi, & A. Santangelo, 65
- McCammon, D., Almy, R., Apodaca, E., et al. 2002, *ApJ*, **576**, 188
- Mpetha, C. T., Collins, C. A., Clerc, N., et al. 2021, *MNRAS*, **503**, 669
- Nagai, D., Kravtsov, A. V., & Vikhlinin, A. 2007, *ApJ*, **668**, 1
- Nandra, K., Barret, D., Barcons, X., et al. 2013, ArXiv e-prints [arXiv:1306.2307]
- Navarro, J. F., Frenk, C. S., & White, S. D. M. 1997, *ApJ*, **490**, 493
- Rosselli, D., Marulli, F., Veropalumbo, A., Cimatti, A., & Moscardini, L. 2023, *A&A*, **669**, A29
- Sarazin, C. L. 1988, *X-ray Emission from Clusters of Galaxies* (Cambridge: Cambridge University Press)
- Sato, K., Uchida, Y., & Ishikawa, K. 2023, ArXiv e-prints [arXiv:2303.01642]
- Simionescu, A., Zuhone, J., Zhuravleva, I., et al. 2019, *Space. Sci. Rev.*, **215**, 24
- Smith, R. K., Brickhouse, N. S., Liedahl, D. A., & Raymond, J. C. 2001, *ApJ*, **556**, L91
- Takahasi, H., & Mori, M. 1974, *Publ. Res. Inst. Math. Sci.*, **9**, 721
- Tashiro, M., Maejima, H., Toda, K., et al. 2020, in *Space Telescopes and Instrumentation 2020: Ultraviolet to Gamma Ray*, eds. J. W. A. den Herder, S. Nikzad, & K. Nakazawa, *SPIE Conf. Ser.*, **11444**, 1144422
- Turner, M. J. L., Abbey, A., Arnaud, M., et al. 2001, *A&A*, **365**, L27
- van der Velden, E. 2020, *J. Open Source Softw.*, **5**, 2004
- Verner, D. A., Ferland, G. J., Korista, K. T., & Yakovlev, D. G. 1996, *ApJ*, **465**, 487
- Walker, S., & Lau, E. 2022, in *Handbook of X-ray and Gamma-ray Astrophysics*, eds. C. Bambi, & A. Santangelo, 13
- Wilms, J., Brand, T., Barret, D., et al. 2014, in *Space Telescopes and Instrumentation 2014: Ultraviolet to Gamma Ray*, *SPIE Conf. Ser.*, **9144**, 1775
- Wojtak, R., Hansen, S. H., & Hjorth, J. 2011, *Nature*, **477**, 567
- XRISM Science Team 2022, ArXiv e-prints [arXiv:2202.05399]
- Zhu, H., Alam, S., Croft, R. A. C., Ho, S., & Giusarma, E. 2019, ArXiv e-prints [arXiv:1901.05615]

Appendix A: An analytical formula for δ_c in the case of a gNFW density profile

Let us recall the expression for the density contrast, δ_c :

$$\delta_c = \frac{M_\delta}{\int_0^{R_\delta} \frac{4\pi r^2 \rho_{\text{crit}}(z)}{(r/r_s)^\gamma (1+r/r_s)^{3-\gamma}} dr} \quad (\text{A.1})$$

By using the expression for the gNFW density provided in [Zhu et al. \(2019\)](#) and noting that :

$$\int x^{2-\gamma} (1+x)^{\gamma-3} dx = \frac{x^{3-\gamma} {}_2F_1(3-\gamma, 3-\gamma; 4-\gamma, -x)}{3-\gamma} + \text{const.} \quad (\text{A.2})$$

where ${}_2F_1$ is the hyper-geometric function. We obtain the following formula for δ_c :

$$\delta_c = \frac{M_\delta}{\frac{4\pi r_s^3 \rho_{\text{crit}}(z)}{3-\gamma} {}_2F_1(3-\gamma, 3-\gamma; 4-\gamma, -c_\delta) c_{200}^{3-\gamma}} \quad (\text{A.3})$$

Appendix B: Simulations without background

The results presented in Sec. 4.1 are obtained for simulations including astrophysical and instrumental background. We ran the simulations in the same setup, however without background, and ran the same analysis as presented in Sec. 3. The results are shown in Fig. B.1. For the observations with high exposure times, such as shown in the upper panel of Fig. B.1, the background has little to no impact, and the constraints obtained over the parameters are identical to those in Fig. 7. For observations with lower exposure times, however, the background is more predominant, and the difference between the cases with and without background is clearer. In particular, mixed exposure 2 shows a smaller extent and is best centered on the real values. From these plots we conclude that the background can have a significant impact on the quality of the redshift fit and therefore on using the redshift profile as a probe for the gravitational redshift.

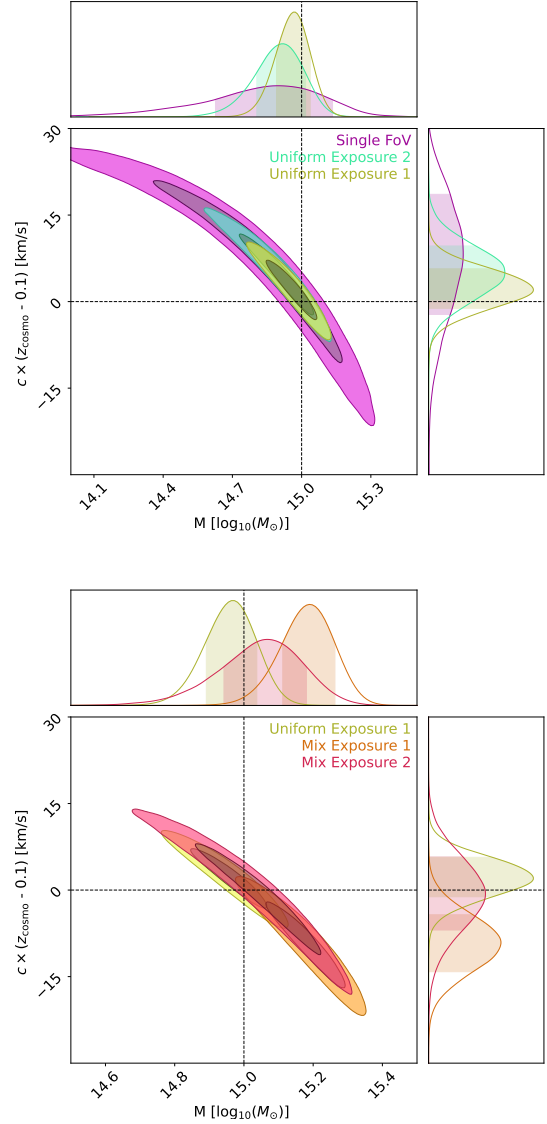


Fig. B.1. Corner plot in the mass and redshift plane and associated posterior distribution for both parameters. The different colors correspond to the different observing strategies listed in the legend and presented in Fig. 1. Top: Uniform exposures 1 and 2, compared with a single pointing observation. Lower: Mixed exposures 1 and 2, compared with a single pointing observation. The input reference values are plotted as dotted lines.

Appendix C: Fitting a line centroid with a binned observation

Here, we attempt to explain the discretization of the likelihood with respect to the position of the emission line center (in the context of the observation of a line through any type of instrument that counts flux in discretized bins). This situation arises whenever the line width becomes equivalent or smaller than the bin width of the instrument measuring the flux. We generated line counts emitted by lines of different widths. For each line, we discretized these counts in bins, as is done with real data. Incoming photons are counted in energy bins to create the spectrum. Then, we broadened these fake line spectra by an arbitrary instrument response, of width slightly larger than the largest of the lines. This provides fake observations. For each line, we constructed a Gaussian line model and process it through the binning and instrument response in the same way as the "observed" counts are. Then, using Poisson statistics, we mapped out the likelihood with respect to the Gaussian line center, assuming the original line width is known. For lines with a width much lower than the instrument bin width, we show that the likelihood is not smooth anymore and has steps, the width of which approaches the bin width (see Figure C.1). Lines of small width with respect to the bin width do not affect the likelihood when their center is moved within the bins, thereby creating steps in the likelihood. In the context of fitting the line center, the likelihood minimum becomes quite ill-defined, as is the associated uncertainties on the extracted parameter.

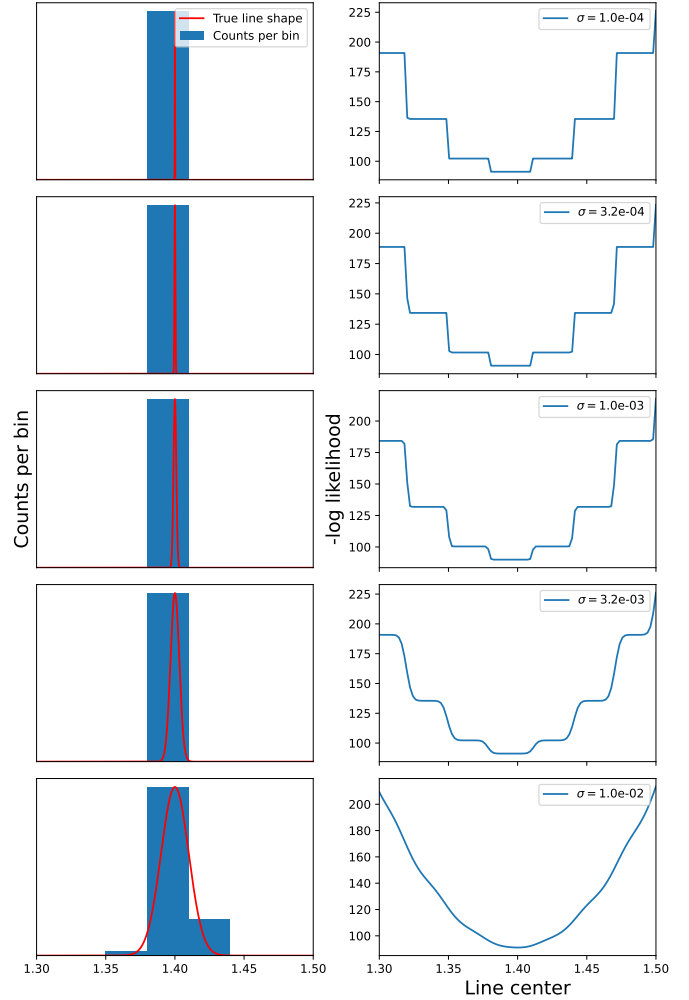


Fig. C.1. Illustration of the discretization occurring in the likelihood of a Gaussian model with respect to the line centroid when the line width is smaller than the binning of the data. Left: Counts per bin as well as true line shape, as a function of energy, in the instrument for lines of different shapes, before instrumental broadening. The qualitative purpose of this plot allows for the use of arbitrary units on the vertical axis. Right: Likelihood of the Gaussian line model with respect to the line center, associated to the line observed in the left panel.